J. Fluid Mech. (2007), *vol.* 573, *pp.* 247–263.
doi:10.1017/S0022112006003818 Printed in the United Kingdom

Hydraulic jumps due to oblique impingement of circular liquid jets on a flat horizontal surface

R. P. KATE, P. K. DAS AND SUMAN CHAKRABORTY†

Department of Mechanical Engineering, Indian Institute of Technology, Kharagpur 721302, India

(Received 6 June 2005 and in revised form 31 July 2006)

An obliquely inclined circular water jet, impinging on a flat horizontal surface, confers a series of hydraulic jump profiles, pertaining to different jet inclinations and jet velocities. These jump profiles are non-circular, and can be broadly grouped into two categories, based on the angle of jet inclination, ϕ, made with horizontal. Jumps corrosponding to the range ($25^\circ < \phi \leqslant 90^\circ$) are observed to be bounded by smooth curves, whereas those corresponding to $\phi \leqslant 25^\circ$ are characterized by distinct corners. The present work attempts to find a geometric and hydrodynamic characterization of the spatial patterns formed as a consequence of such non-circular hydraulic jump profiles. Flow-visualization experiments are conducted to depict the shape of demarcating boundaries between supercritical and subcritical flows, and the corresponding radial jump locations are obtained. Theoretical calculations are also executed to obtain the radial locations of the jumps with geometrically smooth profiles. Comparisons are subsequently made between the theoretical predictions and the experimental observations, and a good agreement between these two can be observed. Jumps with corners, however, turn out to be comprised of strikingly contrasting profiles, which can be attributed to the 'jump–jet' interaction and the 'jump-jump' interaction mechanisms. A phenomenological explanation is also provided, by drawing an analogy from the theory of shock-wave interactions.

1. Introduction

Normal impingement of jets on surfaces is an established technique for providing high local heat/mass transfer rates in a variety of applications, including glass manufacturing, paper drying, gas turbine cooling and electronic packaging. It is well-known that the circular hydraulic jump is a consequence of the normal impingement of circular liquid jets on a flat horizontal surface. Physics of flow patterns obtained under these conditions have been relatively well studied. Figure 1(*a*)(i) illustrates a typical circular hydraulic jump due to a normal impinging jet, while the corresponding experimental visualization is depicted in figure 1(*a*)(ii). Following the pioneering studies of Glauert (1956), Bradshaw & Love (1959), Abramovich (1963), Watson (1964) and Rajaratnam (1976), it can be inferred that the flow field due to normal impinging jets can be divided into three main regions, namely, the free jet region, the impingement region, and the wall jet region. The latter two regions have been further grouped into five sub regions, labelled S_1, S_2, S_3, S_4 and S_5 in figure 1(*c*). The five subregions have been classically termed as the region of boundary-layer-type flow, the region of fully developed flow, the region immediately before the hydraulic jump, the region of the hydraulic jump, and the region downstream of the jump,

† Author to whom correspondence should be addressed: suman@mech.iitkgp.ernet.in

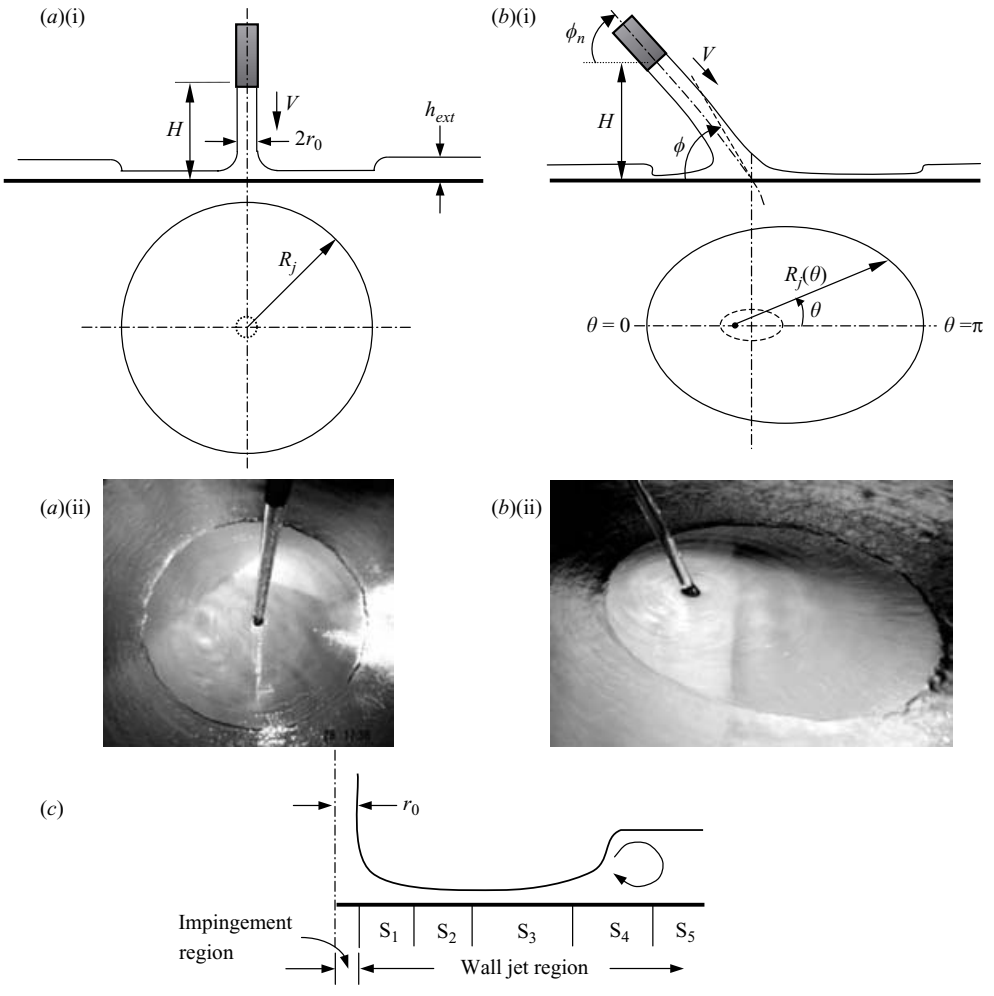

FIGURE 1. Illustrative sketches for (*a*)(i) Normal impinging jet, and (*b*)(i) oblique impinging jet. (*a*)(ii) The circular hydraulic jump (circular liquid jet impinging normal to the horizontal surface), volume flow rate of water, $Q = 1 \times 10^{-4}\,\mathrm{m^3\,s^{-1}}$, nozzle diameter, $d = 8.8\,\mathrm{mm}$. (*b*)(ii) Non-circular hydraulic jump due to a circular liquid jet impinging obliquely on a horizontal surface, $Q = 1 \times 10^{-4}\,\mathrm{m^3\,s^{-1}}$, $d = 8.8\,\mathrm{mm}$, nozzle inclination (with horizontal), $\phi_n = \pi/4$. (*c*) Regions of flow field in the case of a normal impinging jet.

respectively (for details see: Watson 1964; Rao & Arakeri 1998). Various aspects of the circular hydraulic jumps, formed under identical conditions, have been extensively studied (Watson 1964; Olsson & Turkdogan 1966; Ishigai *et al.* 1977; Nakoryakov, Pokusaev & Troyan 1978; Craik *et al.* 1981; Bohr, Dimon & Putkaradze 1993; Godwin 1993; Liu & Lienhard 1993; Higuera 1994, 1997; Blackford 1996; Hansen *et al.* 1997; Brechet & Néda 1999; and Bush & Aristoff 2003). Oblique impinging jets, in comparison to normal impinging jets, however, have received relatively less attention in the fluid mechanics literature. Figure 1(*b*)(i) schematically describes an oblique impinging jet and the associated hydraulic jump characteristics, with the corresponding photographic view depicted in figure 1(*b*)(ii). The obliquity of the jet turns out to be a major parameter in determining the nature of the flow in the case of such non-circular hydraulic jumps, primarily in the following respects. First, the

axial symmetry exists only up to the free jet region, and the flow, in general, is three-dimensional elsewhere (Beltos 1976; Rubel 1981). Secondly, the impingement region, which is considered to span over the cross-section of the jet for a normal impinging jet, is expected to change in size and shape, as the jet becomes obliquely inclined to the horizontal surface. Further, the stagnation point in the impingement zone is no more coincident with the geometrical centre of the jet. An upstream shift of the stagnation point from the geometrical centre of the non-circular impingement zone for oblique impinging jets has been reported in the studies of Beltos (1976), Sparrow & Lovell (1980), Stevens & Webb (1991), Rubel (1981, 1982) and Tong (2003). The radial flow originating from this eccentric stagnation point leads to non-circular hydraulic jump profiles, which is a fundamentally complicated fluid dynamic phenomenon. To the best of our knowledge, even elementary theories for quantitative characterization of the spatial patterns formed as a consequence of such non-circular hydraulic jumps, supported by requisite validation experiments, are yet to be reported in the literature. The aim of the present work, accordingly, is to develop a fundamental understanding of the geometrical features of non-circular hydraulic jumps, formed as a consequence of oblique impingement of circular liquid jets from both experimental and theoretical perspectives, with a quantitative characterization of the pertinent spatial patterns formed.

The outline of this paper is as follows. In § 2, laboratory experiments for the circular and non-circular hydraulic jumps will be discussed. In § 3, a theoretical analysis for the location of the stagnation point will be elaborated. Prediction of radial locations for non-circular hydraulic jumps will subsequently be made, and these results will be further compared with the data obtained from experiments. Hydraulic jumps with corners will be discussed in § 4. In § 5, concluding remarks based on the present study will be outlined.

2. Experiments, flow visualization and observations

The experimental set-up consists of a closed-loop water-jet system, comprised of a centrifugal pump (0.5 h.p., head 30/6 m, capacity 15/40 l min^{-1}, 2800 r.p.m.), two rotameters calibrated in the range of 1.67×10^{-5}—1.67×10^{-4} m^3 s^{-1} and 1.67×10^{-5}—3.33×10^{-4} m^3 s^{-1}, and circular tubes of brass and stainless steel (in the diameter range 4–10 mm). These tubes can be used as nozzles having a length to diameter ratio of 150–200, so as to ensure a fully developed flow condition at the exit. The jet issuing from the nozzle is made to fall on a square glass plate of dimensions 1 m $\times$ 1 m, and a thickness of 8 mm, mounted on four levelling screws. The edge of the glass plate is chamfered with a radius of approximately 4 mm on the top face, for smooth drainage of the liquid. The set-up is fabricated such that that the jump can be viewed and photographed from underneath of the glass plate. Calibration of the experimental set-up has been performed by employing benchmark (experimental) data available in the literature for circular hydraulic jumps. Figure 2 compares the present experimental results with the experimental results of Arakeri & Rao (1996). The figure also shows some of the theoretically predicted estimates of the radius of the jump, using the scaling relations developed by Bohr *et al.* (1993), Godwin (1993) and Brechet & Néda (1999), under identical conditions, for the sake of completeness. As can be seen from figure 2, our experimental results are in good agreement with theoretical predictions obtained from the scaling relations developed by Bohr *et al.* (1993), and experimental results of Arakeri & Rao (1996).

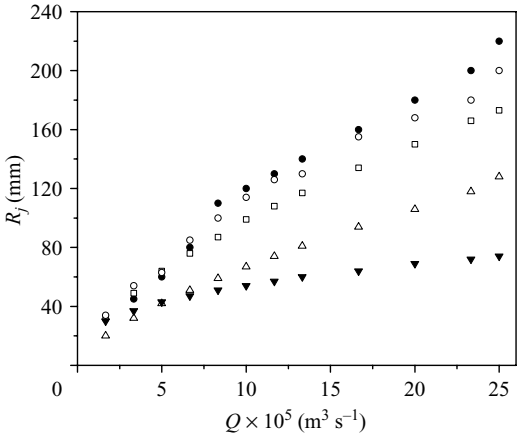

FIGURE 2. The radius of the circular hydraulic jump (R_j) as a function of the volume flow rate of water (Q). ●, experiments (nozzle diameter, $d = 10$ mm) (Arakeri & Rao 1996); □, theory (Bohr *et al.* 1993); △, theory (Brechet & Neda 1999); ▼, theory (Godwin 1993); ○, present experiments ($d = 10$ mm).

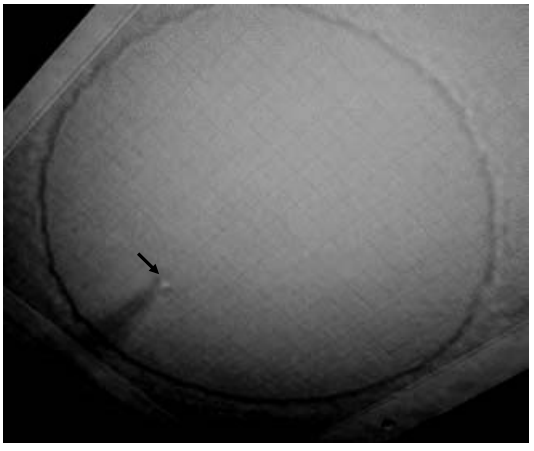

FIGURE 3. The jump profile is measured using graph paper. A shadow of the jump and impingement point (indicated with an arrow) is clearly visible.

Flow visualization is carried out using a digital camera (SONY DSC-F717, Sony Electronics NJ). A 1000 W light source is used for illumination from the top. The impingement point and the inner edge of the separation eddies are clearly visible, signifying the pertinent jump locations, and are marked on transparent graph sheets (containing square meshes of 1 mm resolution) pasted on the underside of the glass plate (figure 3). From our flow visualization experiments, we summarize that the jump profiles due to obliquely inclined impinging jets can be broadly catagorized as follows: (*a*) jumps bounded by a smooth curve (jumps formed when $\phi > 25°$), and (*b*) jumps with corners (jumps formed when $\phi \leqslant 25°$). As ϕ becomes less than 90°, the radial symmetry of the hydraulic jump is lost and it assumes an oblate shape. However, the curve describing this jump is smooth, and we can identify an axis of symmetry passing through the point of impingement ($\theta = 0$) and $\theta = \pi$, where θ is the azimuthal location of a point on the hydraulic jump profile (see figure 1*b*). The jump profile

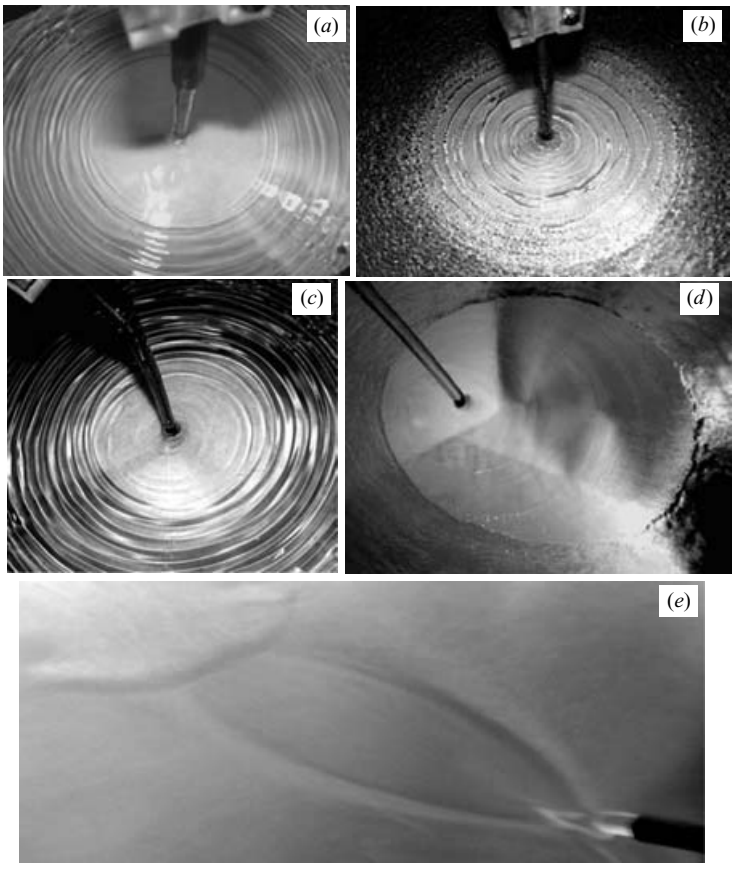

FIGURE 4. Hydraulic jumps at different flow rates, and nozzle inclination angles. (*a*) $Q = 3.33 \times 10^{-5}\ \mathrm{m^3\ s^{-1}}$, $d = 10\ \mathrm{mm}$, (*b*) $Q = 1.17 \times 10^{-4}\ \mathrm{m^3\ s^{-1}}$, $d = 10\ \mathrm{mm}$, (*c*) $Q = 3.33 \times 10^{-5}\ \mathrm{m^3\ s^{-1}}$, $d = 8.8\ \mathrm{mm}$, $\phi_n = \pi/4$, (*d*) $Q = 1 \times 10^{-4}\ \mathrm{m^3\ s^{-1}}$, $d = 8.8\ \mathrm{mm}$, $\phi_n = \pi/4$, (*e*) unique hydraulic jump observed at $\phi_n = 18^\circ$, $H = 9\ \mathrm{mm}$, $d = 6.45\ \mathrm{mm}$ and $Q = 4.17 \times 10^{-5}\ \mathrm{m^3\ s^{-1}}$.

elongates progressively with an increase of V, and decrease in ϕ. It can be noted here that for $\phi > 25^\circ$, changes in V can merely alter the slenderness of the jump profile, without creating any corner. However, for $\phi \leqslant 25^\circ$, in our experiments, a series of unique jump profiles are observed. These profiles have one or more corners, and their shapes are highly sensitive to the variation of V. Typical hydraulic jumps, both due to normal and oblique impinging jets are depicted in figure 4. The hydraulic jumps at lower flow rates are observed to be steady and distinct (figure 4*a*, *c*). However, jumps at relatively higher flow rates are unsteady and ill-defined (figure 4*b*, *d*). During our experiments, the jet Reynolds number (Re_d)is observed to be in the range of 4000 to 25 000. Within this regime, transition to turbulence does not occur. However, beyond $Re_d = 26\,000$ it is observed that the circular hydraulic jump loses its radial symmetry and the corresponding non-circular hydraulic jump loses its axial symmetry. Analysis of hydraulic jumps formed as a consequence of oblique impingement of such turbulent liquid jets, however, remains beyond the scope of present study, and therefore, is not further discussed here.

In contrast to the circular hydraulic jumps, it is found that for inclined impinging jets, the drop height, H, implicitly plays a consequential role in determining the size and shape of the non-circular hydraulic jump. Gravity effects deflect the jet in such

cases, so that the jet angle, (ϕ), becomes greater than the nozzle angle (ϕ_n), as can be seen in figure 2(b). This effect is more pronounced for larger drop heights and at lower flow rates. It can be shown that ϕ, ϕ_n and V are related as:

$$\phi = \tan^{-1}\left[\frac{\left(V^2\sin^2\phi_n + 2gH\right)^{1/2}}{V\cos\phi_n}\right]. \tag{2.1}$$

The value of ϕ obtained using (2.1) is used in further calculations reported in this study. In this context, once this effective angle of jet obliquity is ascertained, any further significance of the drop height, H, becomes practically irrelevant in terms of imposing an explicit influence on the mechanism of the hydraulic jump formed.

3. Theoretical analysis

3.1. *Characterization of the stagnation point for jumps bounded by a smooth curve*

The present theoretical analysis borrows its basic outline from the earlier considerations of Bradshaw & Love (1959), Scholtz & Trass (1970), Looney & Walsh (1984), Bouainouche, Bourabaa & Desmet (1997), and Phares, Smedley & Flagan (2000). In effect, in the present study, an inviscid outer-flow analysis is coupled with the boundary-layer approximations for prediction of radial locations of non-circular hydraulic jumps. The analysis primarily deals with the consequence of an oblique impingement of a circular jet of radius r_0 (diameter, d) impinging on a stationery horizontal plate with V as the velocity of jet impingement. After impingement, the fluid flows radially with velocity V_r. The distribution of this radial flow is uneven, the flux being the highest in the forward flow direction and the lowest in the backward flow direction. The stagnation point, here, is considered to be the point of intersection of the separation streamline with the plane of the impinging surface (figure 5a). The section of this jet, on a plane parallel to the plate, turns out to be an ellipse, of major axis ($2r_0/\sin\phi$), and minor axis ($2r_0$), as shown in figure 5(b). Figure 5(c) shows the top view of the radially spreading flow, along with the section of the jet on the target plate. The origin of the radial flow is located at the stagnation point, S. Assuming a steady flow and neglecting the effects of gravity, surface tension and viscosity, we can write an expression for mass conservation across the shaded element depicted in figure 5(c) as

$$(r_e\mathrm{d}\theta)\,\frac{r_e}{2}\,(V\sin\phi) = \left(r_p\mathrm{d}\theta\right)hV_r, \tag{3.1}$$

where, $r_e = r_e(\phi,\theta)$ is the polar radius of the envelope of the impingement region, and r_p is the radial distance of a point located on the plate (relative to the point S), and h is the film thickness. Further, from mechanical energy balance, it follows that the velocity V is equal to V_r. Hence, (3.1) can be expressed as

$$hr_p = \frac{r_e^2}{2}\sin\phi. \tag{3.2}$$

Now, equating the forward momentum (in the X-direction) transmitted by the jet with the net X momentum generated in the radial flow, we obtain

$$\pi r_0^2 V^2\varrho\cos\phi = \int_0^{2\pi}(hr_p)\varrho V_r^2\cos\theta\,\mathrm{d}\theta, \tag{3.3}$$

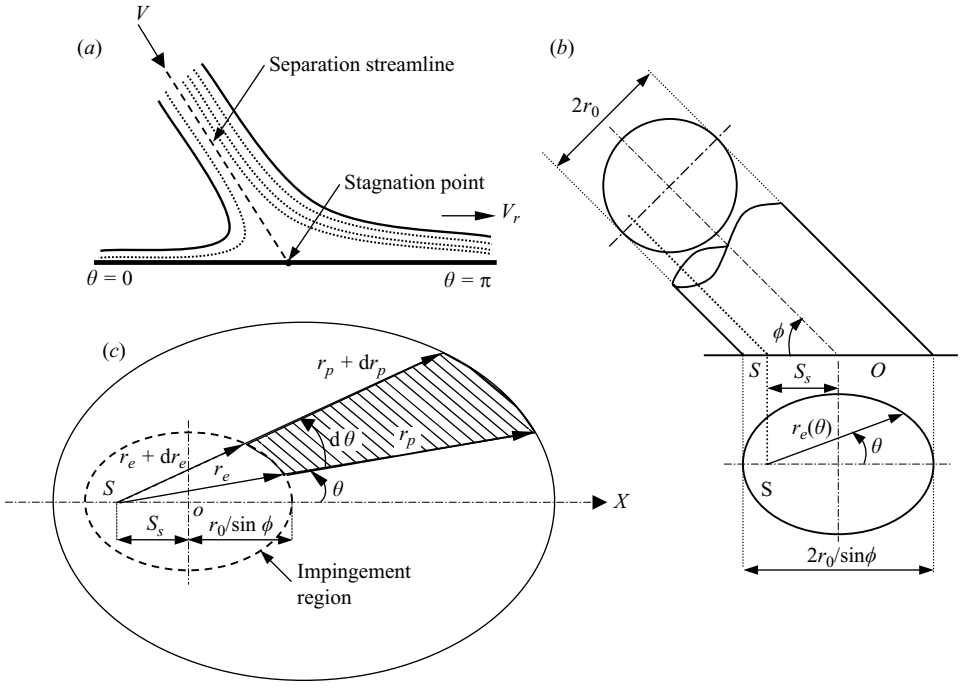

FIGURE 5. (*a*) The stagnation point, the point of intersection of the separation streamline with the plane of the impinging surface. (*b*) The section of the circular jet, on a plane parallel to the plate is an ellipse. (*c*) The top view of the radially spreading flow along with the section of the jet on a plate.

where ϱ is the density of liquid. From (3.2) and (3.3), we obtain

$$\pi \cot\phi = \int_0^{\pi} \left(\frac{r_e}{r_0}\right)^2 \cos\theta \, d\theta. \tag{3.4}$$

Further, the polar equation of the outer boundary of the impingement zone is given as

$$\left(\frac{r_e}{r_0}\sin\theta\right)^2 + \left(\frac{r_e}{r_0}\cos\theta - \frac{S_s}{r_0}\right)^2 \sin^2\phi = 1, \tag{3.5}$$

where S_s is the stagnation point shift (i.e. the distance of the stagnation point from the geometrical centre of the jump profile, O). Obtaining an expression for r_e/r_0 from (3.5) and using the same in (3.4), it can be shown that

$$S_s = r_0 \cot\phi. \tag{3.6}$$

It can now easily be inferred from the above analysis that the polar radius of the non-circular impingement zone, with respect to the stagnation point (which is an upstream focus of the impingement zone) is given by

$$r_e(\phi, \theta) = r_0\left(\frac{\sin\phi}{1 + \cos\phi\cos\theta}\right). \tag{3.7}$$

3.2. *Radial locations, $R_j(\theta)$, of non-circular hydraulic jump*

As mentioned in § 3.1, the impingement zone of the inclined circular jet can be modelled as an impingement zone of an equivalent vertical elliptic jet, which is

approximately of the size of the elliptic jet itself. The radially spreading flow in this case will be three-dimensional in its nature. This three-dimensional nature of the flow can be modelled effectively as a pseudo two-dimensional one by considering the coordinate r itself as a function of θ. Further simplifications are made by assuming that surface tension effects are negligible in comparison to gravity effects. Moreover, gradients along the axial directions are assumed to be much more dominant in comparison to those along the radial directions, consistent with the prevailing length scales. Using these considerations, the pertinent equations of continuity and momentum in cylindrical coordinates can be written as:

$$\frac{\partial V_r}{\partial r} + \frac{V_r}{r} + \frac{\partial V_z}{\partial z} = 0, \tag{3.8a}$$

$$V_r \frac{\partial V_r}{\partial r} + V_z \frac{\partial V_r}{\partial z} = -g \frac{\mathrm{d}h}{\mathrm{d}r} + \nu \frac{\partial^2 V_r}{\mathrm{d}z^2}, \tag{3.8b}$$

where $V_r(r, z)$ and $V_z(r, z)$ are the components of the velocity in the radial and vertical directions, respectively, $h(r)$ is the thickness of the fluid layer, and g is the acceleration due to gravity. Equations (3.8a) and (3.8b) are consistent with the following boundary conditions:

$$V_r(r, 0) = 0, \tag{3.9a}$$

$$V_z(r, 0) = 0, \tag{3.9b}$$

where $r = r(\theta)$.

$$\left[\frac{\partial V_r}{\partial z}\right]_{z=h(r)} = 0, \tag{3.9c}$$

$$r \int_0^h V_r(r, z)\,\mathrm{d}z = q, \tag{3.9d}$$

where $q = Q/2\pi$, Q being the volume flow rate (as the product of rhV_r happens to be an invariant function with respect to θ). The coordinate r, which is itself a function of θ, is measured with respect to the source of the radially spreading flow.

Equations (3.8a) and (3.8b) are now re-written in a dimensionless form using typical scales for the radial velocity V_r^*, vertical velocity V_z^*, radius r^* and thickness of the liquid layer z^*, with the following substitutions:

$$V_r = \alpha V_r^*, \qquad \alpha = q^{1/8}\nu^{1/8}g^{1/8}, \tag{3.10a}$$

$$V_z = \beta V_z^*, \qquad \beta = q^{-1/4}\nu^{3/4}g^{1/4}, \tag{3.10b}$$

$$r = \gamma r^*, \qquad \gamma = q^{5/8}\nu^{-3/8}g^{-1/8}, \tag{3.10c}$$

$$z = \delta z^*, \qquad \delta = q^{1/4}\nu^{1/4}g^{-1/4}. \tag{3.10d}$$

Rescaled equations (dropping asterisks) are then obtained as

$$\frac{\partial V_r}{\partial r} + \frac{V_r}{r} + \frac{\partial V_z}{\partial z} = 0, \tag{3.11a}$$

$$V_r \frac{\partial V_r}{\partial r} + V_z \frac{\partial V_r}{\partial z} = -\frac{\mathrm{d}h}{\mathrm{d}r} + \frac{\partial^2 V_r}{\mathrm{d}z^2}. \tag{3.11b}$$

The boundary conditions in terms of rescaled quantities can be described as

$$V_r(r, 0) = 0, \tag{3.12a}$$

where $r = r(\theta)$,

$$V_z(r, 0) = 0, \tag{3.12b}$$

$$\left[\frac{\partial V_r}{\partial z}\right]_{z=h(r)} = 0, \tag{3.12c}$$

$$r \int_0^{h(r)} V_r(r, z)\, \mathrm{d}z = 1. \tag{3.12d}$$

Although the boundary-layer analysis break, down in a small region around the point of separation, the rest of the flow can be described well by following such approximations. The system of averaged equations in the z-direction, however, avoids showing the singular behaviour at the point of separation and can adequately describe the flow pattern involving the separation of the boundary layer in an integrated sense. Integrating (3.11b) over z from 0 to $h(r)$, and simultaneously exploring the continuity equation (3.11a), we obtain (after incorporating boundary conditions (3.12a) to (3.12d)):

$$\frac{1}{rh}\frac{\mathrm{d}}{\mathrm{d}r}\left[r \int_0^h {V_r}^2\, \mathrm{d}z\right] = -h' - \frac{1}{h}\frac{\partial V_r}{\partial z}\,|_{z=0}, \tag{3.13}$$

where the prime denotes differentiation with respect to r.

Now, define:

$$F_2 = \int_0^h \left(\frac{V_r}{V_{av}}\right)^2 \mathrm{d}z, \tag{3.14}$$

where V_{av} is the average velocity, defined as

$$V_{av} = \frac{1}{h}\int_0^h V_r(r, z)\, \mathrm{d}z. \tag{3.15}$$

Further, conservation of mass yields

$$V_{av} hr = 1. \tag{3.16}$$

From equations (3.13) to (3.16), we obtain:

$$V_{av}(F_2 V_{av})' = -h' - \frac{1}{h}\frac{\partial V_r}{\partial z}\,|_{z=0}\,. \tag{3.17}$$

For further simplifications, a judicious choice of the velocity profile must be made. In this context, it can be noted here that the classical von Kármán and Pohlhausen method for boundary-layer analysis assumes a velocity profile that is ascertained purely by the external flow conditions (Schlichting 1960). Here, however, the thickness of the fluid film, $h(r)$, plays a role that is very much analogous to the boundary-layer thickness in a classical viscous flow analysis, in terms of dictating the exact self-similar nature of the velocity profile. Accordingly, one may write

$$\frac{V_r(r, z)}{V_{av}} = f(\eta), \tag{3.18}$$

where $\eta = z/h(r)$ and V_{av} is the average velocity, satisfying (3.16). Since the velocity profile must also satisfy the boundary conditions (3.12a) to (3.12d) and (3.16), $f(\eta)$ must obey the following restraints:

$$f(0) = 0, \tag{3.19}$$

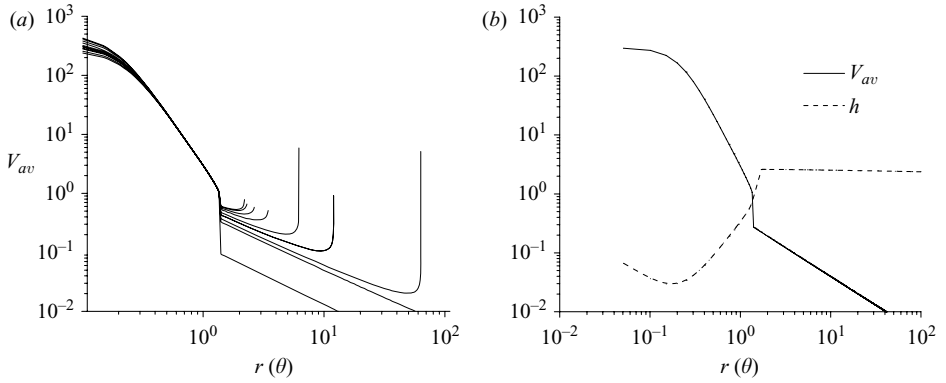

FIGURE 6. (*a*) Numerical solution of the equation (3.25), (*b*) typical solution for V_{av} and h, which is indicative of a characteristic discontinuity at $r(\theta) \approx 1$.

$$f'(1) = 0, \tag{3.20}$$

$$\int_0^1 f(\eta)\,\mathrm{d}\eta = 1. \tag{3.21}$$

For example, a quadratic profile

$$f(\eta) = 3\eta - \tfrac{3}{2}\eta^2, \tag{3.22}$$

may be one of the simplest possible polynomial forms for the function f, satisfying (3.19) to (3.21). Then, from (3.14), $F_2 = 6/5$, is obtained as a constant, and (3.17) becomes

$$\tfrac{6}{5} V_{av} V_{av}' = -h' - \frac{3V_{av}}{h^2}. \tag{3.23}$$

Any other valid ansatz for f will still lead to the same form as (3.23), except for the numerical coefficients. There is no qualitative change, however, since all equations of the type (3.23), corresponding to different profile shapes, $f(\eta)$, can be further transformed to a general form:

$$V_{av} V_{av}' + h' = \frac{-V_{av}}{h^2}, \tag{3.24}$$

after suitable rescaling of h, v and r. Combining equations (3.16) and (3.24), we obtain

$$V_{av}'\left(V_{av} - \frac{1}{{V_{av}}^2 r}\right) = \frac{1}{V_{av} r^2} - {V_{av}}^3 r^2. \tag{3.25}$$

Typical solutions of (3.25) are shown in figure 6. At large enough values of $r(\theta)$, the velocity suddenly increases, which corresponds to a sudden drop in height. This singularity is interpreted physically as the end of the plate where the water runs off (Bohr *et al.* 1993). The above solution for the flow field after the jump can be connected to the solution before the jump by means of a Rayleigh shock, which conserves mass and momentum flux given as follows:

$$V_{av1} h_1 = V_{av2} h_2, \tag{3.26a}$$

$$h_1\left({V_{av1}}^2 + \frac{g h_1}{2}\right) = h_2\left({V_{av2}}^2 + \frac{g h_2}{2}\right), \tag{3.26b}$$

Velocity profile	Approximate value of C
$\frac{8}{3}\eta - \frac{4}{3}\eta^3$	0.76
$\frac{20}{9}\eta - \frac{5}{9}\eta^4$	0.83
$\frac{15}{7}\eta - \frac{3}{7}\eta^5$	0.85

TABLE 1. Numerical value of constant C (equation (3.27)) for higher-order velocity profiles.

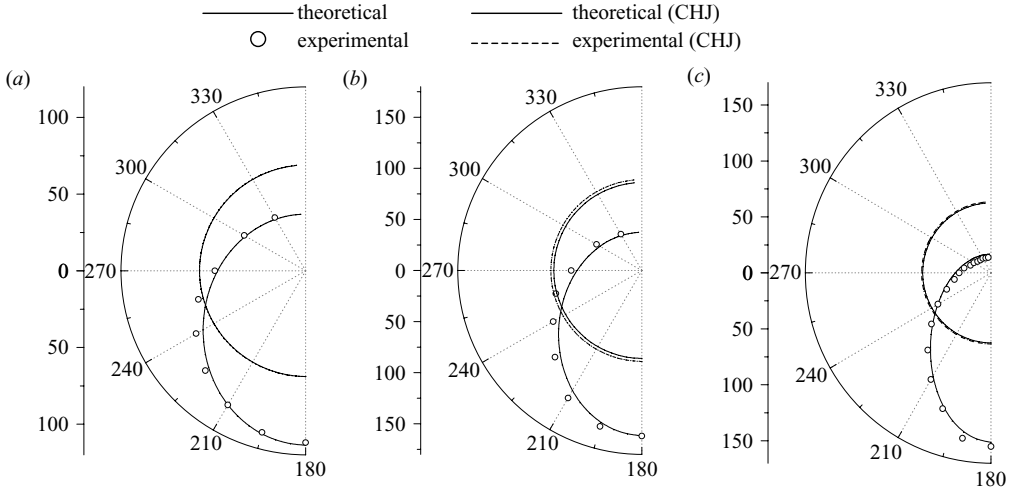

FIGURE 7. Radial locations, $R_j(\theta)$ of the hydraulic jumps for different values of nozzle angles (ϕ_n) and flow rates (Q): (*a*) $r_0 = 3.5\,\text{mm}$, $Q = 5.83 \times 10^{-5}\,\text{m}^3\,\text{s}^{-1}$, $\phi_n = 60°$, $H = 56\,\text{mm}$ (*b*) $r_0 = 4.35\,\text{mm}$, $Q = 8.33 \times 10^{-5}\,\text{m}^3\,\text{s}^{-1}$, $\phi_n = 45°$, $H = 80\,\text{mm}$, (*c*) $r_0 = 3.25\,\text{mm}$, $Q = 5 \times 10^{-5}\,\text{m}^3\,\text{s}^{-1}$, $\phi_n = 35°$, $H = 40\,\text{mm}$.

where, subscripts 1 and 2 correspond to values before and after the jump. Since the above shock (which can be interpreted as a hydraulic jump, in the present case) occurs very close to $r(\theta) = 1$ (in the dimensionless coordinates), the radial location of the jump, $R_j(\theta)$, scales approximately as r^*, and is given from (3.10*c*) as

$$R_j = \gamma = Cq^{5/8}\nu^{-3/8}g^{-1/8}. \tag{3.27}$$

Here, the constant C depends on the velocity profile chosen in (3.14). For a parabolic profile, for example, C turns out to be approximately 0.73. For higher-order profiles, satisfying the requisite boundary conditions (equations (3.19) to (3.21)), the respective values of C are shown in table 1. Further, for the present case, q can be expressed as

$$q = \frac{Q}{(2\pi)} = rh(\theta)V_r. \tag{3.28}$$

From equations (3.2), (3.7) and (3.28), we obtain, at $r_p = r_e$

$$q = rh(\theta)V = \frac{{r_0}^2}{2}\left[\frac{\sin^3\phi}{(1+\cos\phi\cos\theta)^2}\right]V. \tag{3.29}$$

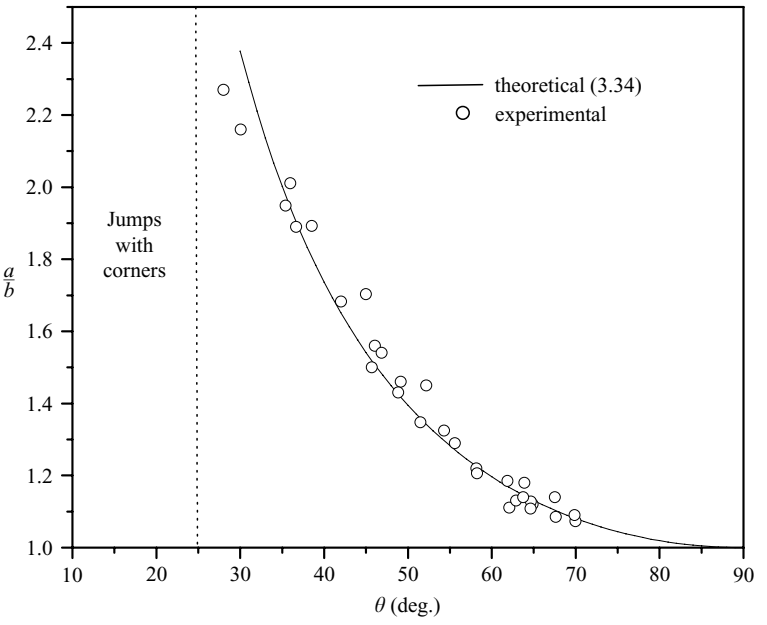

FIGURE 8. Aspect ratio (ratio of major axis, a, to minor axis, b) of non-circular hydraulic jumps is independent of V for a fixed ϕ.

With this value of q, radial locations of the jump $R_j(\phi, \theta)$ are obtained as

$$R_j(\phi, \theta) = C \left[\frac{{r_0}^2}{2} \frac{\sin^3\phi}{(1 + \cos\phi \cos\theta)^2} V \right]^{5/8} \nu^{-3/8} g^{-1/8}. \tag{3.30}$$

As a special case, the radius of the circular hydraulic jump can be obtained by putting $\phi = \pi/2$ in equation (3.30), as

$$R_j = C \left(\frac{{r_0}^2 V}{2} \right)^{5/8} \nu^{-3/8} g^{-1/8}, \tag{3.31}$$

which can also be written as

$$R_j = C q^{5/8} \nu^{-3/8} g^{-1/8}. \tag{3.32}$$

Equation (3.32) is essentially the same as that developed by Bohr *et al.* (1993), which shows that the instance of a circular hydraulic jump can be obtained as a special case from the present generalized theory.

A comparison of experimental results and the present theoretical predictions is shown in figure 7. Experimental results are in extremely good agreement with the corresponding theoretical predictions for the hydraulic jumps bounded by a smooth curve. Predictions regarding circular hydraulic jumps (CHJ), ($\phi = \pi/2$), are also plotted on the same figure, for effective comparisons. It can be shown that the aspect ratio (ratio of the major axis, a, to the minor axis, b) of the non-circular hydraulic jump is given by

$$\frac{a}{b} = \frac{1}{(1 - \cos^2\phi)^{5/8}}. \tag{3.33}$$

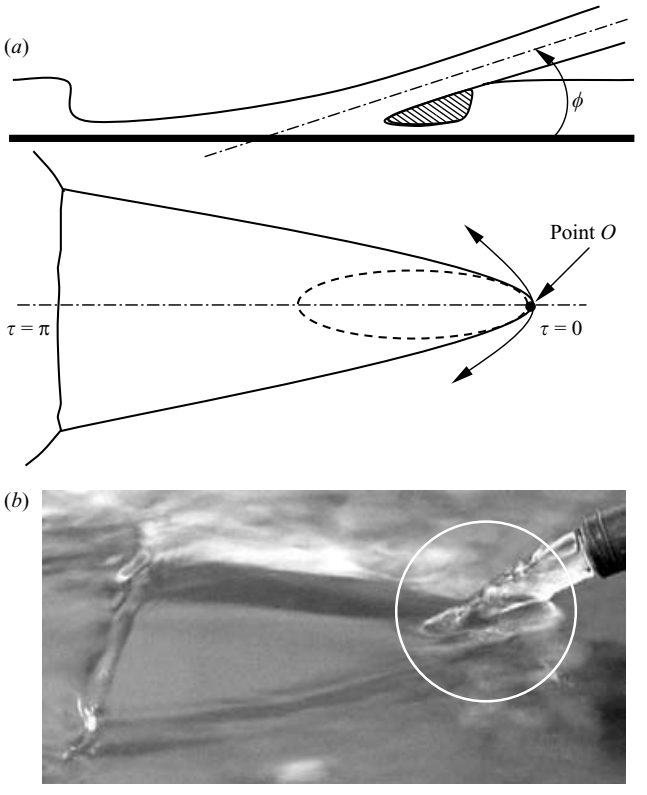

FIGURE 9. (*a*) Illustrative sketch of jump–jet interaction. (*b*) Jet–jump interaction (encircled) observed during our experiments. This interaction perturbs the flow leading to cornered hydraulic jumps.

Hence, the aspect ratio is a function of ϕ only, and is independent of V, as mentioned in § 2. Variations in aspect ratio with ϕ, as obtained using (3.33) and from our laboratory experiments, are shown in figure 8.

4. Hydraulic jumps with corners

A series of jump profiles with altogether different shapes emerge for $\phi \leqslant 25^\circ$. At these values of ϕ, the elliptic impingement zone elongates substantially such that the jump profile at the extreme upstream position ($\theta = 0$) makes a contact with the impinging jet (see figure 9). This confluence, termed the 'jump–jet interaction', is dependent on parameters ϕ, V and d. The upstream location of the impingement zone, which now coincides with the extreme upstream of the jump profile, becomes somewhat pointed, as depicted in figure 9 (refer to the point O in figure 9*a*). From this point, two identical branches of jump emerge. At the vicinity of the impingement zone, the fluid undergoes a 'shooting flow', with a relatively high velocity. This makes two branches of the jump diverge from each other. However, the two branches are curved, as is the boundary of the impingement zone itself. Further downstream, the two branches come closer. Depending on the distance between the branches and their strengths, different interactions may be possible. These interactions can be termed as the 'jump–jump interactions'. At a relatively low impingement velocity, the jump profile shape more or less conforms to isosceles triangular shapes (figure 10(*a*(i), (ii)

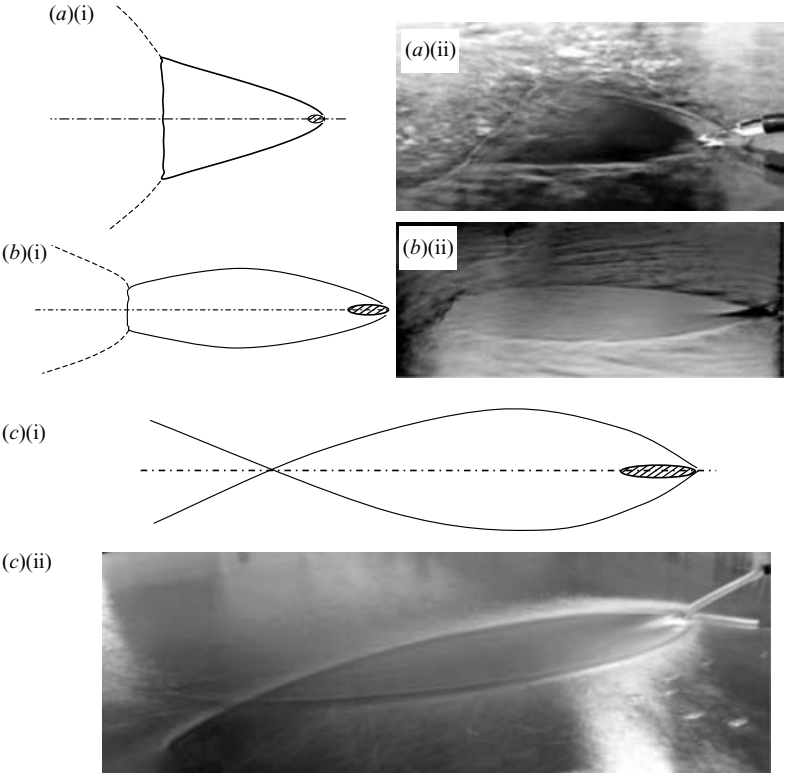

FIGURE 10. Hydraulic jump with corners: (*a*)(i), (*b*)(i) and (*c*)(i) are type I, type II and type III jump profiles, respectively, (*a*)(ii) ($\phi_n = 17.5°$, $Q = 5 \times 10^{-5}\ \mathrm{m^3\ s^{-1}}$, $d = 6.48\ \mathrm{mm}$, $H = 11\ \mathrm{mm}$), (*b*)(ii) ($\phi_n = 17.5°$, $Q = 8.33 \times 10^{-5}\ \mathrm{m^3\ s^{-1}}$, $d = 6.48\ \mathrm{mm}$, $H = 11\ \mathrm{mm}$), and (*c*)(ii) ($\phi_n = 17.5°$, $Q = 1.25 \times 10^{-4}\ \mathrm{m^3\ s^{-1}}$, $d = 6.48\ \mathrm{mm}$, $H = 11\ \mathrm{mm}$) are the corresponding cornered jumps visualized in our experiments.

(type I jumps)), the vertex of the triangle being located at the extreme upstream point of the jump profile. Additionally, we observed the formation of wave structures and disturbances beyond the base (side opposite to the extreme upstream) of the triangle, as can be seen in figure 10(*a*)(i).

With an increase in V, the extreme upstream of the jump becomes more pointed. The two equal sides of the jump profile elongate and become curved. The base takes a bow shape and its length decreases. The typical form observed can be described as a 'tear drop' shape (figure 10*b*(i), (ii)) (type II jumps). With further increases in V, the two branches of the jump profile, emerging from the extreme upstream point come closer to each other. At one point, the third branch (i.e. the branch perpendicular to the line of symmetry) disappears and the other two branches intersect each other, giving the jump profile a typical shape. The shape now resembles that of a fish (figure 10*c*(i), (ii)) (type III jump). With any increase in V beyond this, the profile elongates and encompasses a greater area. However, the jump profile shape remains unaltered. Figure 11 depicts the qualitative changes in the hydraulic jump profiles with the corrosponding variations in ϕ and V. Disturbances and waves of a secondary nature have also been observed beyond the third branch and at the point of intersection of the branches (except at the extreme upstream point)(see figures 10*a*(ii) and *b*(ii)).

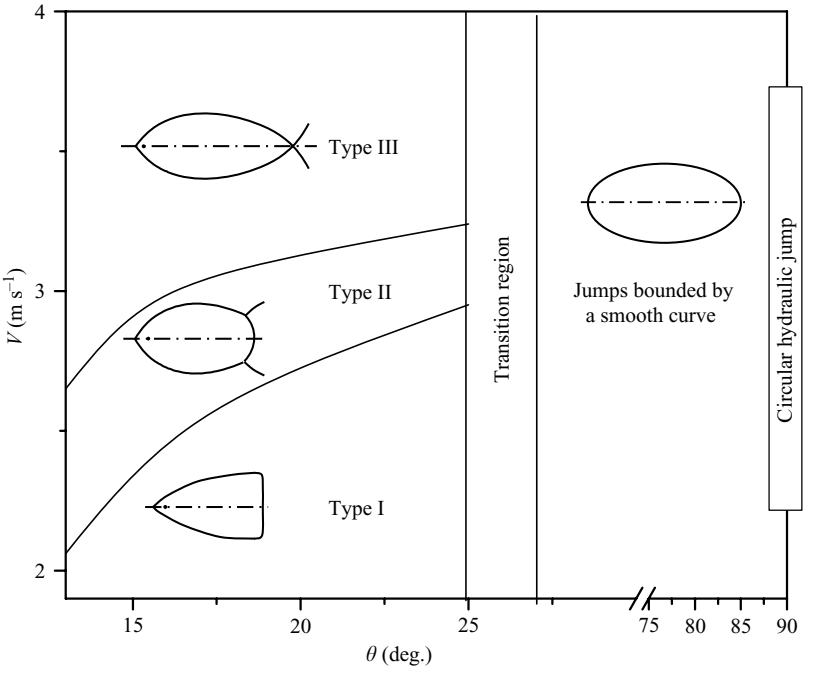

FIGURE 11. Phase diagram for hydraulic jumps due to obliquely impinging circular liquid jet on a flat horizontal surface, ($d = 6.45$ mm, $H = 9$ mm).

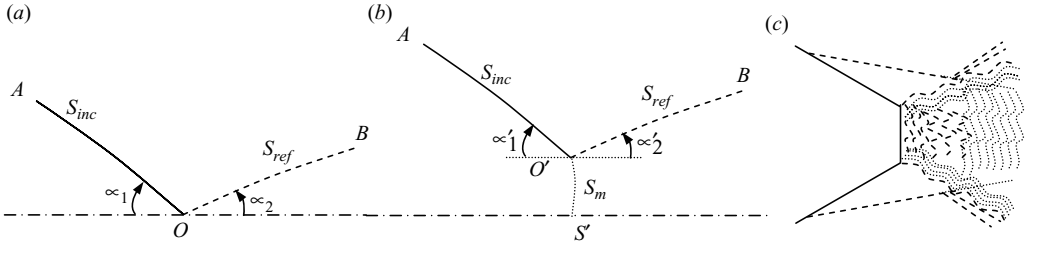

FIGURE 12. Shock reflections: (*a*) regular reflection, and (*b*) Mach reflection, S_{inc} and S_{ref} are incident and reflected shocks, respectively, and S_m is the Mach stem. (*c*) Waves and structures of a secondary nature in shock reflections.

Qualitative phenomenological explanations for the formation of such non-intuitive hydraulic jump profiles can be provided by appealing to the similarity between a hydraulic jump and a compression shock (Preiswerk 1940). When two oblique waves meet each other, the axis of symmetry passing through the meeting point conceptually acts as an impervious wall. One of the shocks may be considered to be incident on that wall, while the other is reflected. Two types of reflection, namely regular reflection and Mach reflection (figure 12), have been reported to characterize these situations. In Mach reflection, the incident wave and the reflected wave meet at a point away from the axis of the symmetry. A third wave, known as a Mach stem, joins this point with the axis of symmetry. The Mach stem is, in general, curved at the triple point. The entire stem may also be curved, depending on the characteristics of the interacting waves. Further, waves and structures of a secondary nature are observed downstream

of the Mach stem (figure 12*c*). Similar interactions between discontinuity waves in shallow-water flows have been observed by Gilmore, Plesset & Crossley (1950).

The hydraulic jump profiles with corners (figure 10) can be explained in light of regular and Mach reflections mentioned as above (refer to figure 12). Formation of the triangular jump profile (type I) corresponds to the case of a Mach reflection, where the base of the triangle is nothing but a Mach stem. With further development, the Mach stem becomes shorter, as observed in type II profiles. Eventually, a case of regular reflection occurs as the flow rate is further increased, leading to a complete disappearance of the Mach Stem in type III profiles. Waves and structures of a secondary nature (see figures 10*a*(ii) and *b*(ii), similar to those encountered in compressible gasdynamics beyond the shock wave interactions, have also been observed during the present experiments.

5. Summary and conclusions

In this paper, we have studied hydraulic jumps that occur when circular impinging jets fall on a smooth horizontal plate at different angles of obliquity. Changes in the flow field of an impinging jet owing to its inclination are analysed from both theoretical and experimental perspectives. It has been revealed that the circular impingement zone deforms to an equivalent elliptic one. The stagnation point, consequently, shifts to the upstream focus of the elliptical impingement zone. The analysis for the radial locations of the non-circular hydraulic jump profile (jumps bounded by a smooth curve), based on this conjucture, gives satisfactory predictions, as evident from the favourable comparisons with experimental observations. For jumps with corners, which form at lower angles of jet inclination, strikingly contrasting profiles can be obtained, for which a phenomenological explanation is provided by drawing analogies from shock-wave interactions.

REFERENCES

Abramovich, G. N. 1963 *The Theory of Turbulent Jets* (ed. L. H. Schindel). MIT Press.

Arakeri, J. H. & Rao, A. 1996 On radial flow on a horizontal surface and the circular hydraulic jump. *J. Indian Inst. Sci.* **76**, 73–91.

Beltos, S. 1975 Oblique impingement of circular turbulent jets. *J Hydraul. Res.* **14**, 17–36.

Blackford, B. L. 1996 The hydraulic jump in radially spreading flow: a new model and new experimental data. *Am. J. Phys.* **64**, 164–169.

Bohr, T., Dimon, P. & Putkaradze, V. 1993 Shallow-water approach to the circular hydraulic jump. *J. Fluid Mech.* **254**, 635–648.

Bouainouche, M., Bourabaa, N. & Desmet, B. 1997 Numerical study of the wall shear produced by the impingement of a plane turbulent jet on a plate. *Intl J. Numer. Meth. Heat Fluid Flow.* **7**, 548–564.

Bradshaw, P. & Love, E. M. 1959 The normal impinging jet of a circular air jet over a flat surface. *ARC R &M 3205*. Aero. Res. Council, UK.

Brechet, Y. & Néda, Z. 1999 On the circular hydraulic jump. *Am. J. Phys.* **67**, 723–731.

Bush, J. W. M. & Aristoff, J. M. 2003 The influence of surface tension on the circular hydraulic jump. *J. Fluid. Mech.* **489**, 229–238.

Craik, A., Lathman, R., Fawkes, M. & Gibbon, P. 1981 The circular hydraulic jump. *J. Fluid. Mech.* **112**, 347–362.

Gilmore, F. R., Plesset, M. S. & Crossley Jr, H. E. 1950 The analogy between hydraulic jumps in liquids and shock wave in gases. *J. Appl. Phys.* **21**, 243–249.

Glauart, M. B. 1956 The wall jet. *J. Fluid. Mech.* **1**, 625–643.

Godwin, R. 1993 The hydraulic jump ('shocks' and viscous flow in the kitchen sink). *Am. J. Phys.* **61**, 829–832.

Hansen, S. H., Horlúck, S., Zauner, D., Dimon, P., Ellegaard, P. & Watanabe, S. 1997 Geometrical orbits of surface waves from a circular hydraulic jump. *Phy. Rev.* E **55**, 7048–7061.

Higuera, F. J. 1994 Hydraulic jump in a viscous laminar flow. *J. Fluid Mech.* **274**, 69–92.

Higuera, F. J. 1997 The circular hydraulic jump. *Phys. Fluids* **9**, 1476–1478.

Ishigai, S., Nakanishi, S., Mizunao, M. & Imamura, T. 1977 Heat transfer of the impinging round water jet in the interference zone of film flowing along the wall. *Bull. JSME* **20**, 85–92.

Liu, X. & Lienhard, J. 1993 The hydraulic jump in circular jet impingement and in other thin liquid films. *Exps. Fluids* **15**, 108–116.

Looney, M. K. & Walsh, J. J. 1984 Mean-flow and turbulent characteristics of free and impinging jet flow. *J. Fluid Mech.* **147**, 397–429.

Nakoryakov,V., Pokusaev, B. & Troyan, E. 1978 Impingement of an axisymmetric liquid jet on a barrier. *Intl J. Heat Mass Transfer* **21**, 1175–1184.

Olsson, R. G. & Turkdogan, E. T. 1966 Radial spread of a liquid stream on a horizontal plate. *Nature* **211**, 813–816.

Phares, D. J., Smedley, G. T. & Flagan, R. C. 2000 The wall shear stress produced by the normal impingement of a jet on a flat surface. *J. Fluid Mech.* **418**, 351–375.

Preiswerk, E. 1940 Applications of the methods of gas dynamics to water flows with free surfaces. *NACA TM* 934 and 935.

Rajaratnam, N. 1976 *Turbulent Jets.* Elsevier.

Rao, A. & Arakeri, J. H. 1998 Integral analysis applied to radial film flows. *Intl J. Heat Mass Transfer* **41**, 2757–2767.

Rubel, A. 1981 Computations of the oblique impingement of round jets upon a plane wall. *AIAA J.* **19**, 863–871.

Rubel, A. 1982 Oblique impingement of a round jet on plane surface. *AIAA J.* **20**, 1756–1758.

Schlichting, H. 1960 *Boundary Layer Theory*. McGraw-Hill.

Scholtz, M. T. & Trass, O. 1970 Mass transfer in nonuniform impinging jet. *AIChE J.* **16**, 82–90.

Sparrow, E. M. & Lovell, B. J. 1980 Heat transfer characteristics of an obliquely impinging circular jet. *Trans. ASME C: J. Heat Transfer* **102**, 202–209.

Stevens, J. & Webb, B. W. 1991 The effect of inclination on local heat transfer under an axisymmetric free liquid jet. *Intl J. Heat Mass Transfer* **34**, 1227–1236.

Tong, A. Y. 2003 On the oblique impingement heat transfer of an oblique free surface plane jet. *J. Heat Mass Transfer* **46**, 2077–2085.

Taylor, G. 1960 Formation of thin flat sheets of water. *Proc. R. Soc. Lond.* A **259**, 1–17.

Watson, E. J. 1964 The spread of a liquid jet over a horizontal plane. *J. Fluid Mech.* **20**, 481–499.

Yokoi, K. & Xiao, F. 2002 Mechanism of structure formation in circular hydraulic jumps: numerical studies of strongly deformed free-surface shallow flows. *Physica* D **161**, 202–219.